applied sciences

MDPI

Article

Regulated Power Supply with High Power Factor for Hyperspectral Imaging Applications

Jose M. Cabrera-Peña [1,*], Raquel Leon [1], Samuel Ortega [1,2,3,*], Himar Fabelo [1,4,5], Eduardo Quevedo [1] and Gustavo M. Callico [1]

[1] Research Institute for Applied Microelectronics (IUMA), University of Las Palmas de Gran Canaria (ULPGC), 35017 Las Palmas de Gran Canaria, Spain; slmartin@iuma.ulpgc.es (R.L.); hfabelo@iuma.ulpgc.es (H.F.); eduardo.quevedo@ulpgc.es (E.Q.); gustavo@iuma.ulpgc.es (G.M.C.)
[2] Nofima—Norwegian Institute of Food Fisheries and Aquaculture Research, NO-9091 Tromsø, Norway
[3] Department of Mathematics and Statistics, UiT The Arctic University of Norway, NO-9091 Tromsø, Norway
[4] Fundacion Canaria Instituto de Investigacion Sanitaria de Canarias (FIISC), 35012 Las Palmas de Gran Canaria, Spain
[5] Research Unit, Hospital Universitario de Gran Canaria Dr. Negrin, 35010 Las Palmas de Gran Canaria, Spain
* Correspondence: jose.cabrera@ulpgc.es (J.M.C.-P.); sortega@iuma.ulpgc.es (S.O.)

Abstract: Illumination is a crucial factor in hyperspectral imaging systems. In this respect, this work is focused on analyzing the influence of the light power source in acquiring hyperspectral images. To this end, a custom regulated power supply was designed and developed. This power supply was then integrated into a hyperspectral acquisition system, and several light stability measurements were conducted. Finally, several parameters related to the stability of the light produced by those systems were extracted using image analysis techniques, and a statistical comparison among the different power supplies was performed. Two commercial power supplies were also analyzed under the same experimental conditions and compared with the proposed power supply. The hyperspectral measurements were conducted using light transmission and reflectance. The results indicate that the proposed power supply performs better than or at least as well as commercial power supplies in terms of light stability. Additionally, this study shows the impact of power supply design on the stability and quality of hyperspectral illumination, especially concerning the signal-to-noise ratio (SNR) across different spectral bands. It is shown that optimizing the design of the power supply could improve light stability in hyperspectral imaging applications.

Keywords: hyperspectral imaging; regulated power supply; power factor; illumination system

Academic Editors: Eduardo Espinosa Neira, Pedro Eduardo Melín Coloma and Ricardo Lizana Fuentes

Received: 10 December 2024
Revised: 10 January 2025
Accepted: 17 January 2025
Published: 22 January 2025

Citation: Cabrera-Peña, J.M.; León, R.; Ortega, S.; Fabelo, H.; Quevedo, E.; Callico, G.M. Regulated Power Supply with High Power Factor for Hyperspectral Imaging Applications. *Appl. Sci.* **2025**, *15*, 1093. https://doi.org/10.3390/app15031093

1. Introduction

Hyperspectral Imaging (HSI) is a technology capable of capturing both the spatial and the spectral information of scenes focused by a hyperspectral (HS) camera. The spectral information for HS applications is usually in the range of the visible and near-infrared regions of the electromagnetic spectrum (typically 400–2500 nm), which allows this technology to overcome the limitations of the human vision. Since the interaction between light and matter is unique for each material, this technology is suitable for identifying materials only based on their spectral information. This characteristic has made this technology attractive for many different fields. Initially, it was developed for remote sensing

applications [1,2]. However, as HSI technology has proven its ability to non-invasively measure the chemical composition of materials, its use has expanded to a wide variety of research and industrial applications. For example, HSI is currently used for food quality inspection [3,4], art restoration [5,6], industrial sorting of materials [7], forensic analysis [8], and medical applications [9,10], among others.

The workflow for these applications typically consists of using HS instruments to collect datasets, and then using various image processing and machine learning techniques to extract useful information from the HS images. A crucial part of this process is the acquisition of the HS data. Data are highly dependent on instrumentation. There are four key elements in every HS acquisition system: (i) the lens used to focus the object to be measured; (ii) the optical element able to separate the incoming light into specific wavelengths; (iii) the electronic sensor to digitalize the information; and (iv) the light source used to illuminate the objects under examination. Each element of the acquisition system affects its overall spectral response [11]. Significantly, the spectral shape of the light source limits the spectral range of the acquisition system, and cameras are required to be stimulated by light sources with a broadband spectral range. Typically, halogen or Xenon-based light sources are employed due to their broadband emission in the visible and infrared regions of the electromagnetic spectrum. Recent studies have compared different light sources, showing that, for specific applications, halogen-based illumination systems work better than LED-based illumination systems in HS image acquisition [12].

Since illumination is a critical factor in HSI systems, some authors have focused their research on measuring the influence of illumination in HSI measurements. These research works cover the influence of the spatial distribution of light [13,14], the light intensity [15], or the spectral shape of the light source [12,16]. In a work that discusses the current calibration problems and their possible solutions in HSI, Geladi et al. defined a list of properties that an ideal illumination system should have for HSI applications [17]. These properties cover, among others, spatial homogeneity over larger areas, broadband emission, and high intensity. However, as far as we are concerned, the influence of the light power source on the acquisition of HS images has not yet been addressed in the scientific literature.

Commercial illumination systems present two main drawbacks. Firstly, the light source is limited in power (max 150 W), which makes it difficult to capture images in scenes where the illumination is poor due to the intermediate optic elements, such as fiber optic light guides for obtaining cold light illumination. As a result, due to the low power of the lighting system, it is sometimes necessary to add more lighting systems to the current one. Secondly, the optimal light intensity used to illuminate the scene to be captured depends on the ambient light conditions. Furthermore, the operator must manually adjust the light power, which results in images being captured under non-optimal conditions. In order to deal with the above limitations, this work presents the development of a stable, programmable, and low-cost regulated power supply for use in HSI instrumentation.

This research contributes to the understanding of how power sources influence the quality and performance of HSI acquisition systems. The primary objective was to systematically explore this relationship, culminating in the design and development of a custom-regulated power supply. The custom power supply was integrated into a HSI acquisition system, and a series of experiments were conducted to assess the stability of the light source. To provide a robust comparative framework, stability measurements were also conducted using two commercially available power supplies. This comparative approach not only emphasizes the performance of the custom solution but also generates valuable benchmarking data. Additionally, image analysis techniques were employed to extract various stability parameters of the light emitted by both the custom and commer-

cial systems. A statistical analysis of the findings revealed the influence of the power supply for enhanced stability in HSI applications. The evaluation of light stability across different wavelengths shows the significant influence of the power supply on the performance of the acquisition system. To the best of our knowledge, this research represents the first comprehensive study of the effects of power supply characteristics on hyperspectral imaging systems, paving the way for improved design and optimization of power sources in such applications.

2. Background Concepts

2.1. Total Harmonic Distortion

The term total harmonic distortion (THD) is a way to define the distortion factor of a signal. This concept refers to the measurement of the quality of a waveform and is defined as the relationship between the harmonic content of the signal ($I_{n,RMS\ IN}$) and the first harmonic ($I_{1,RMS\ IN}$), as it is presented in (1). From the definition of instantaneous current (2), the effective or root mean squared (RMS) current can be defined by (3). For the nth harmonic, the effective value of the current can be calculated using (4). The THD value is a percentage that lies between zero and infinity and, ideally, is as low as possible (close to zero).

$$THD = \frac{\sqrt{\sum_{n=1}^{\infty} I_{n,RMS\ IN}{}^2}}{I_{1,RMS\ IN}} \times 100\% \quad (1)$$

$$i(t) = I \cdot sen(\omega t) \quad (2)$$

$$I_{rms} = \sqrt{\frac{1}{T}\int_0^T i^2(t)\,.\,dt} \quad (3)$$

$$I_{n,rms} = \left(\frac{I_{n,max}}{\sqrt{2}}\right) \quad (4)$$

The harmonic distortion of a signal can be caused by a transient phenomenon, such as the starting of a motor or short circuit failures, or by permanent conditions mainly related to steady-state harmonics. For the latter, standards are established to define the permissible limits of distortion. The presence of undesired harmonics can negatively affect the spectrum of the hyperspectral illumination system and should be reduced.

2.2. Power Factor

The power factor (PF) can be defined as a measure of electrical energy consumption efficiency. PF refers to the relationship between the active or useful power and the apparent or total power provided by the electrical network. Therefore, the PF value falls between 0 and 1. Ideally, this value should always tend to 1, since it would be taking advantage of all the power of the electrical network. However, the real input voltage and current waveforms are not purely sinusoidal and are out of phase. This is because of the large amount of electronic equipment connected to the electricity distribution network. Such loads, which are mainly non-linear, distort the input current of the system and therefore do not correspond to the traditional definition of PF. Figure 1 shows the waveform of the grid voltage (red), which is modified by the inherent resistance of the power supply cables delivering the AC voltage to a power supply unit equipped with a rectifier bridge and capacitor filter. This configuration results in a pulsating current (blue) derived from the grid, which aligns with the charging cycles of the filter capacitor. This current is defined as the repetitive peak current, which increases in magnitude and decreases in duration as the capacitance of the filter capacitor is increased.

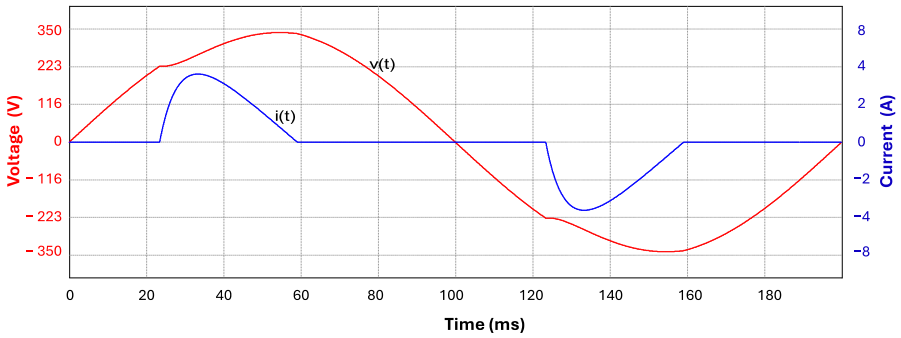

Figure 1. Real input voltage v(t) waveform (red line) affected by a rectified and filtered input current i(t) waveform (blue line).

In order to formally define the PF, the RMS voltage and current values of the nth harmonic ($V_{(n,RMS\ IN)}$; $I_{(n,RMS\ IN)}$) and their phase shifts between them (φ_n) shall be taken into account, as presented in (5), which is the fraction between the active power (P) and the apparent power (S). For sinusoidal voltage $v(t)$ and non-sinusoidal current $i(t)$, the PF can be expressed in a simplified form as presented in (6), where $cos\varphi_1$ is the voltage and current displacement factor (DF, Equation (7)), and *Kp* is the distortion factor defined in (8).

$$PF = \frac{\frac{1}{T}\int_0^T \left(v(t)\cdot i(t)\right)dt}{\frac{1}{T}\int_0^T v(t)^2 dt \cdot \frac{1}{T}\int_0^T i(t)^2 dt} = \frac{\sum_{n=1}^{\infty} V_{n,RMS\ IN} \cdot I_{n,RMS\ IN} \cdot cos\varphi_n}{V_{RMS\ IN} \cdot I_{RMS\ IN}} \quad (5)$$

$$PF = \frac{P}{S} = \frac{V_{1,RMS} \cdot I_{1,RMS} \cdot \cos(\varphi_1)}{V_{RMS} \cdot I_{RMS}} = \frac{I_{1,RMS}}{I_{RMS}} cos(\varphi_1) \quad (6)$$

$$DF = cos(\varphi_1) \quad (7)$$

$$Kp = \frac{1}{\sqrt{1+THD^2}} \quad (8)$$

2.3. Power Supply

The main purpose of a power supply is to provide a voltage value suitable for the operation of any device. To this end, it converts the alternating current input from the network into a continuous (or direct) voltage. This process consists of several stages: *transformation*, *rectification*, *filtering*, and *regulation*. There are mainly two types of power supplies: *linear* (Figure 2a) or *switched* (Figure 2b).

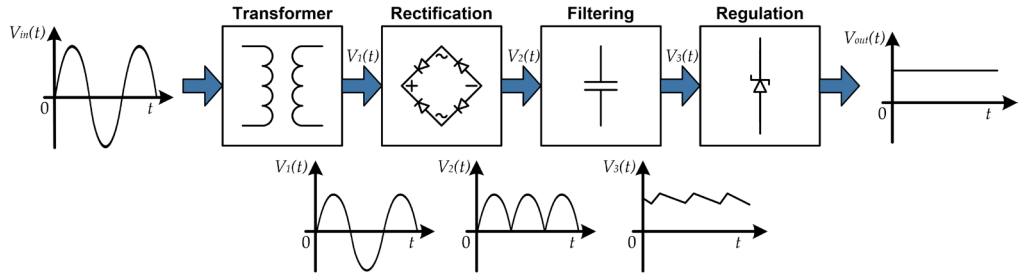

(**a**)

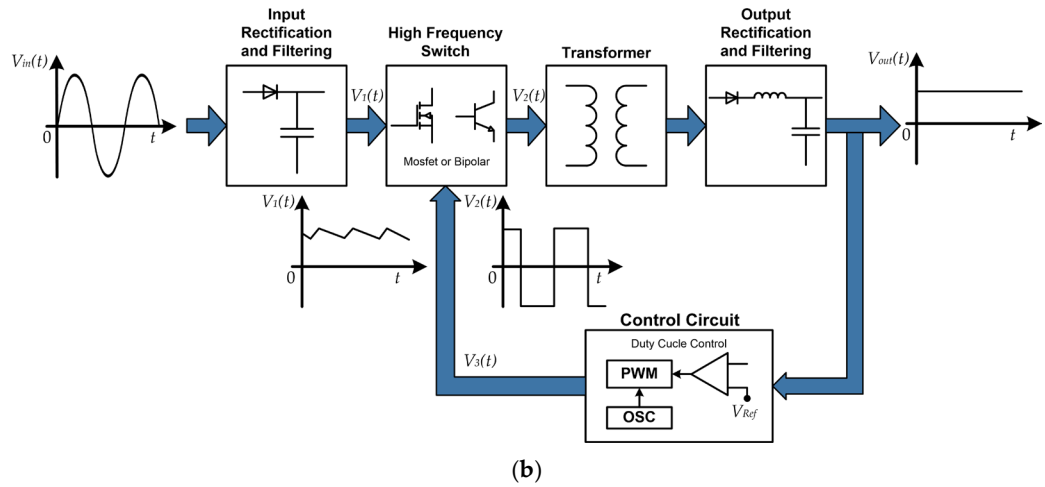

Figure 2. Block diagrams of the two types of power supplies. (**a**) Linear. (**b**) Switched-mode.

A linear power supply (LPS) is a type of power supply that rectifies an alternating current (AC) signal and adjusts its output voltage. It operates by transforming the mains voltage to a lower, desired level using a transformer. This transformer is connected to the mains supply and provides a different output voltage suitable for the intended application. In contrast, a switched power supply directly rectifies the mains voltage and then changes it, usually reducing it, using a transformer switched by switches operating in cut-off or saturation mode.

Each power supply consists of an AC/DC transformation stage based on a full wave rectifier bridge. As mentioned in the previous section, non-linear loads cause harmonic distortion. Rectifiers are an example of this and produce the following adverse harmonic effects:

- Increase in RMS value of the current circulating in the conductors and transformers since it forces the transformers and conductors to be over-dimensioned in order to prevent overheating;
- Increase in losses due to the Joule effect;
- Decrease in the lifespan of transformers and conductors due to overheating;
- Interferences with telecommunications systems;
- Decrease in the power system efficiency;
- Discharge of distorted current into the electrical network, impairing the network's ability to supply energy.

Hence, it is necessary to apply corrective measures to reduce this distortion and consequently improve the PF. In order to comply with current regulations [18] and to counteract the negative effects, a set of solutions should be addressed. A possible solution consists of using semiconductor components, such as transistors (Q) and diodes (D), in addition to passive elements, such as resistors (R), coils (L), and capacitors (C). This solution is based on obtaining a current from the network with a sinusoidal or quasi-sinusoidal waveform. In our proposed solution, we employ a resistance emulator based on the model proposed by Ben-Yaakov, Mordechai-Peretz, and Hesterman [19], as presented in (9), where Rc is the resistance at the cold temperature Tc (assumed to be 300 K), and Th is the temperature of the tungsten filament (450 K in our case). This emulator is a DC/DC converter that, from the point of view of the electrical network side, emulates the behavior of a resistive load. This type of solution provides a PF very close to the maximum and thus a considerable reduction in the harmonic distortion of the input current signal.

$$R_h = R_c \left(\frac{T_h}{T_c}\right)^{1.2285} \quad (9)$$

3. Proposed Circuit Configuration

The main objective of this work can be summarized as follows:

- To develop a switched-mode power supply (SMPS) with automatic PF correction and 25 VDC/20 A as output;
- To provide, at the output, two step-down converters with variable output voltage depending on the needs of the required illumination of the scene. This output should be adjustable from 7 to 21 V. The maximum power of each output should be 150 W;
- To comply with the UNE-EN IEC 61000-3-2:2019 standard [20];
- Two commercial power supplies will be used to compare the PF and performance with respect to the proposed system.

In this work, we propose an SMPS with PFC (Power Factor Correction) and double output from two independent buck converters, shown in Figure 3. The detailed block diagram of the power supply with PFC is shown in Figure 4. As shown in Figure 5, we decided to use a two-stage DC/DC converter, which consists of adding a second stage to the single-stage converter. In the first converter, the PF correction and voltage regulation functions are performed at a fixed value, while the second stage regulates the output voltage and provides a fast dynamic response through a control loop. This structure overcomes the shortcomings of the previous structure and improves its performance by achieving more effective control of the output voltage, reducing its ripple and the sensitivity of the input current to output disturbances [21].

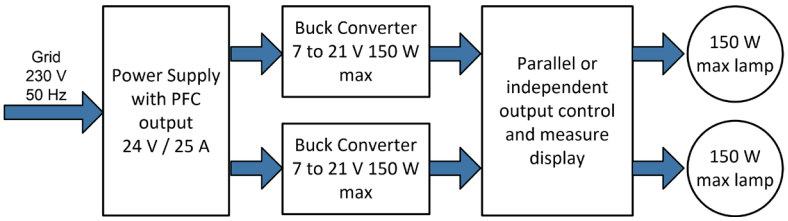

Figure 3. Switching power supply with PFC and double output from two independent buck converters.

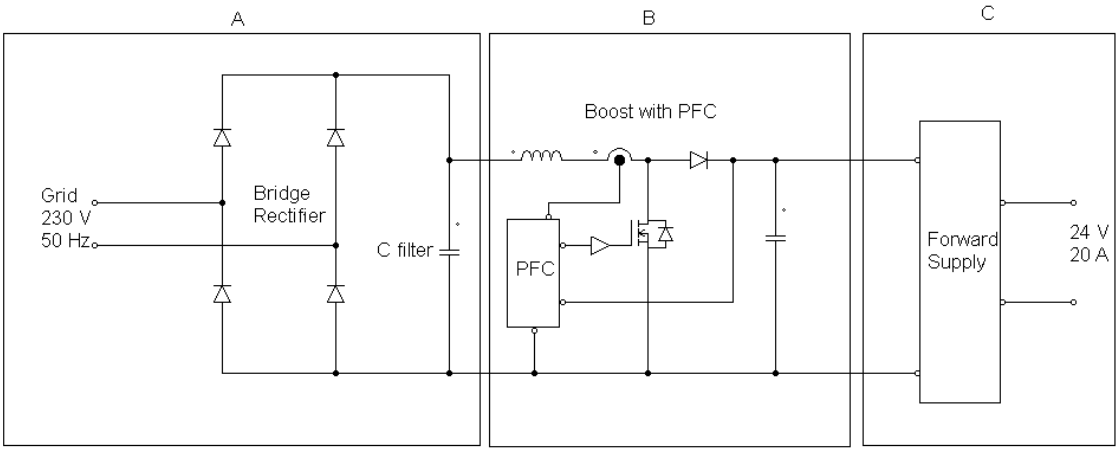

Figure 4. Breakdown of the switching power supply with PFC. (**A**) Uncontrolled rectifier bridge with capacitor filter (**B**) Automatic PF and THD correction using a DC-DC boost converter. (**C**) DC-DC converter with galvanic isolation and automatic output voltage control using forward topology.

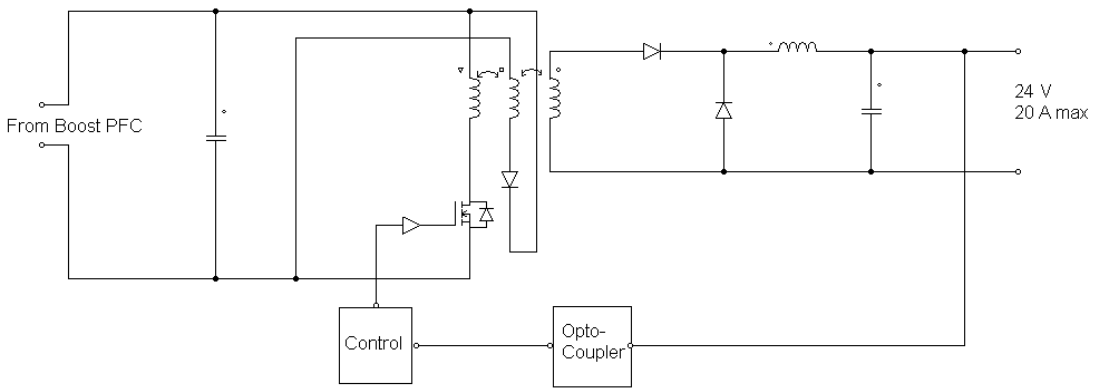

Figure 5. Forward DC/DC converter.

The integration of automatic PFC is a crucial component of this design, as it adjusts the current drawn from the electrical grid to more closely resemble a pure sine wave signal. This modification enhances the efficiency of the equipment and reduces distortion in the power supply. The control of the PF is located just after the diode bridge. Regarding the type of control employed, currently, there is a wide variety of methods devoted to correcting the PF. Generally, two basic control loops are required for any control strategy, as shown in Figure 6. An external voltage loop is used to keep the bus voltage level at a fixed value. An internal current loop controls the current through the coil and forces it to adopt the most similar waveform to the rectified voltage input signal, thus achieving a PF close to the maximum. This integrated circuit is not a simple addition to the PF corrector but integrates the functions of the modulator, the multiplier, and the operational amplifiers of the internal and external loop regulators. For this purpose, the UC3854 contains an analogue voltage amplifier, a multiplier/splitter, a current amplifier, and a fixed frequency PWM (Pulse-Width Modulation) modulator.

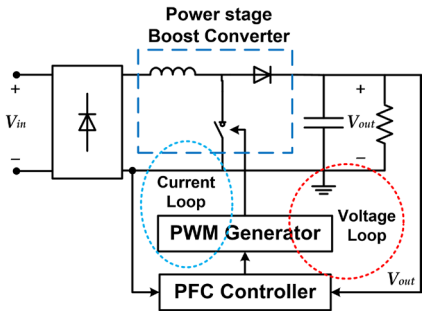

Figure 6. Control scheme of a boost converter.

The implementation of such control loops makes the system stable with a tolerable dynamic behavior regardless of the system load conditions. The power supply developed in this work is part of the lighting equipment and will demand an active input power higher than 500 W. For this reason, it belongs to Class C, and the harmonic currents must not exceed the relative limits indicated in Table 1.

Table 1. IEC 61000-3-2 current harmonic limits for Class C Equipment. λ is the circuit PF.

Harmonic Order (*n*)	Maximum Permissible Harmonic Current (% of Input Current at Fundamental Frequency)
2	2
3	$30 \cdot \lambda^2$
5	10
7	7

9	5
11 ≤ n ≤ 39	3

3.1. Proposed Implementation

The proposed power supply is based on a full-bridge switched mode capable of supplying 500 VA. As shown in Figure 7, the proposed system consists of an automatic PF and THD corrector integrated with the bridge rectifier of the primary voltage and the filtering of the rectified voltage. It follows a double feedback strategy in a boost converter, which samples the input current to the bridge and subsequently regenerates it using the LC filter of the boost converter. The boost converter is kept at a ratio of 1 (*input*) to 1.3 (*output*) to avoid using an inductance with very low resistive losses. This would require increasing the switching frequency to reduce the size of the inductance, losing the energy storage capacity of L, and worsening the final performance of the system, which aims to keep PF close to unity.

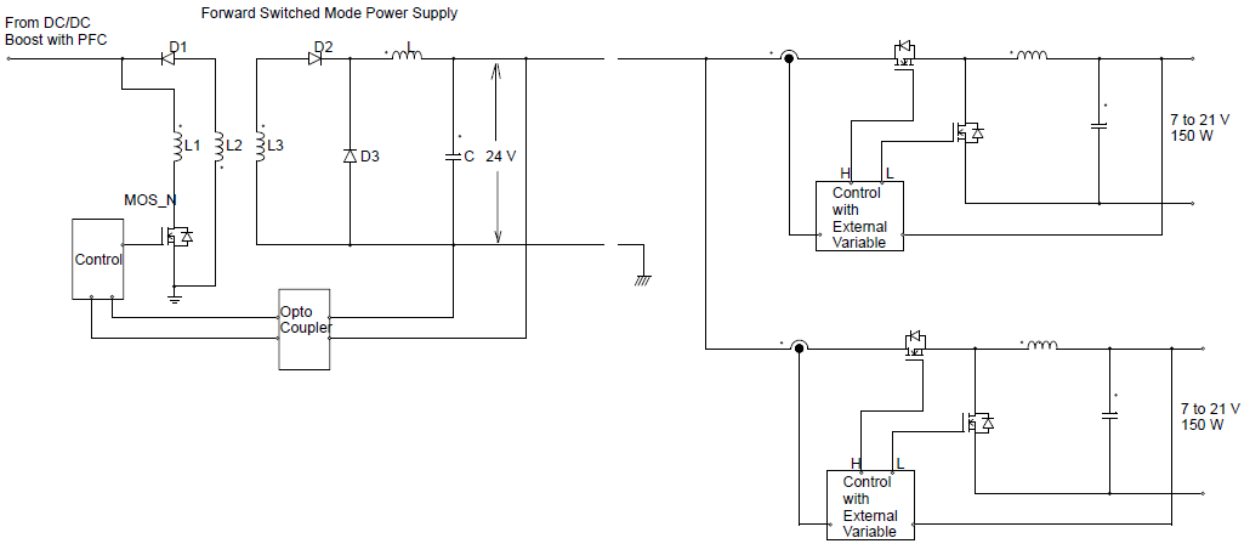

Figure 7. Power supply with two Buck DC/DC converters.

The next stage is a high-frequency transformer switched through a full bridge with low-loss MOSFETs. The duty cycle of these MOSFETs is not critical, as the focus is on ensuring that the dead time between switches is sufficient to avoid the pulses generated by the short circuits due to the simultaneous switching of MOSFETs with opposite switching periods. When the two MOSFETs that were conducting stop, and the other two start, this causes short circuits (in the range of nanoseconds) that result in very high current peaks at very high frequencies that are difficult to filter.

The output of this transformer is filtered by means of a rectifier bridge based on Schottky diodes since the system works at high frequencies and an output filter based on a combination of several high-frequency electrolytic capacitors in parallel.

The regulated voltage is applied to two synchronous variable voltage step-down converters with double feedback (output voltage current given by the MOSFETs, Supplementary Figure S1). This allows us to have two outputs of 150 W each, with the voltage varying between 7 and 21 V independently.

A PCB was built to implement all the components, and it was completely shielded to avoid the emission of electromagnetic interference and achieve the electromagnetic compatibility imposed by the current regulations. Two voltage step-down converters with a controlled output voltage between 7 and 21 V and 150 W of maximum power each were connected to the output of the aforementioned source (Supplementary Figure S1). All this

equipment, in turn, was shielded inside an aluminum box to which were added, among other items, output voltage and current displays.

3.2. Quality Assessment of the Lighthing Systems for Hyperspectral Imaging

The proposed custom power supply and two commercial power supplies were integrated into an HS setup to analyze its performance. The proposed power supply is called PPS in the experiments. The commercial power supplies (CPS) used in this experiment are an MI-150 illuminator (Dolan Jenner Industries Inc., MA, USA), called CPS1 in the experiments (E in Figure 8), and a TechniQuip's Model 21 DC light source (TechniQuip, Pleasanton, CA, USA), called CPS2 in the experiments (C in Figure 8). Both power supplies can generate white light with a light power of 1750 lm using a 150 W Quartz Tungsten halogen lamp, with a mean lifetime between 1000 and 10,000 h. All the power supplies (PPS, CPS1, and CPS2) were connected to two different light sources through fiber optic to measure the light in reflectance and transmittance illumination modes. The first light source is a guide light (B in Figure 8) that emits a line, and it is used in pushbroom HS cameras to capture HS images in reflectance mode. The captures were performed using a white reference tile reflecting 99% of the light (G in Figure 8). The second light source is a backlight illuminator (Dolan-Jenner QVABL fiber optic; F in Figure 8 and is used to capture HS images in transmittance mode. In this case, the HS camera captures the light directly from the backlight.

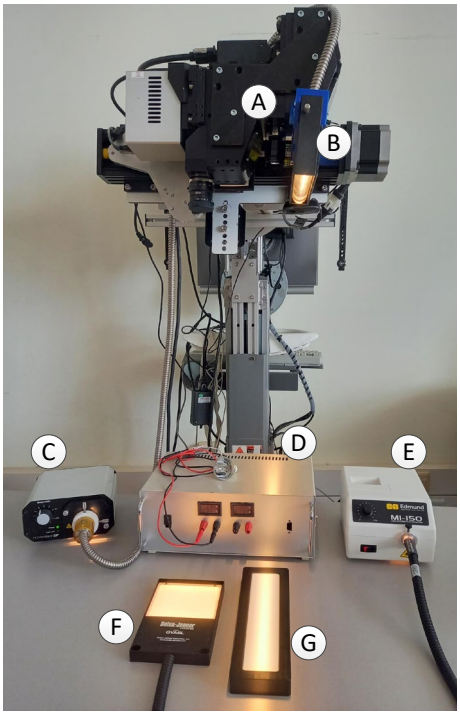

Figure 8. HSI instrumentation. A: Pushbroom camera; B: guide light employed for the light reflectance experiments; C: TechniQuip's commercial power supply (CPS1); D: proposed power supply employed (PPS); E: MI-150 commercial power supply (CPS2); F: backlight illuminator employed in the light transmission experiments; G: white reference tile employed in the light reflectance experiments.

The HS camera used in this study is a pushbroom camera, which means that each frame is composed of one spatial dimension (columns) and all the spectral dimensions (rows). This HS camera is a Hyperspec VNIR A-Series (HeadWall Photonics, Fitchburg, MA, USA; A in Figure 8) and works on the spectral range from 400 to 1000 nm. In traditional pushbroom HS acquisitions, the remaining spatial dimension required to create a

HS cube is obtained by spatial scanning, where either the HS camera or the sample are moved. However, in this research, we are interested in the performance of the light over time. For this reason, the third dimension of the HS cube is composed of repeated measurements of the light. In other words, the third dimension of the HS cube is a temporal profile of the evolution of the light within the experiments.

This research aims to explore the influence of power sources on the quality and performance of HSI instrumentation. Illumination is a key factor in HSI instrumentation; nevertheless, the influence of the power supply in the illumination performance has not been extensively studied in the literature. To address this issue, our investigation emphasizes the importance of short-term stability, as immediate illumination performance is crucial for multiple HSI applications, especially when successive HSIs are sampled in a short time. Two distinct experimental setups were conducted to assess the efficacy of the different power supplies: reflectance and transmittance illumination. The only change in each experimental measurement was to alternate the power supply unit connected to the illumination head (whether in transmission or reflectance mode) while keeping both the HSI instrumentation and the illumination head configuration unchanged to isolate the impact of the power supply type. The power supply developed within this study (PLS) is configured to deliver an output of 150 W. Conversely, the power supplies used as benchmark (CPS1 and CPS2) were adjusted to their respective maximum allowable output power levels. For the different power supplies, the measurements were performed using the same halogen lamp and illumination head. Each measurement involved capturing 500 frames at an exposure time of 40 ms using the VNIR (Visible and Near-Infrared) camera. There is no synchronization between the power sources and the imaging system. For this reason, we manually activated the power supply after about 50 frames during each experimental measurement to capture data from the transient light intensity. The experimental measurements were carried out at room temperature (approximately 25 °C), with each type of power supply being tested ten times to ensure consistency and reliability of the results. From the HS cube, different information can be extracted. Figure 9a,c show the mean information contained in the HS cube from the spatial and spectral dimensions. First, regarding the spatial information (horizontal axis), in Figure 9, it can be observed that the field of view (FOV) of the camera contains light since the white reference used for the reflectance experiment was larger than the FOV. However, that is not the case for the transmittance experiment, where the backlight illumination is smaller than the camera FOV. Therefore, there is no information about light in all the spatial coordinates of the transmittance experiment. This effect can be shown in Figure 9c, where the location of the backlight illumination is approximately contained in the spatial pixels from 250 to 850. Second, the temporal information can be observed in Figure 9b,d. This information was extracted as the mean light intensity of the entire spectral range within the HS cube. From these images, it can be observed that there are three regions. The first rows of the images represent the period when the light is still turned off. Then, once the light is turned on, there are a few rows representing the transition period (transient period) before the light is stabilized (steady period). In this steady period, the light intensity is high and homogeneous for the rest of the rows of the spatio-temporal profile.

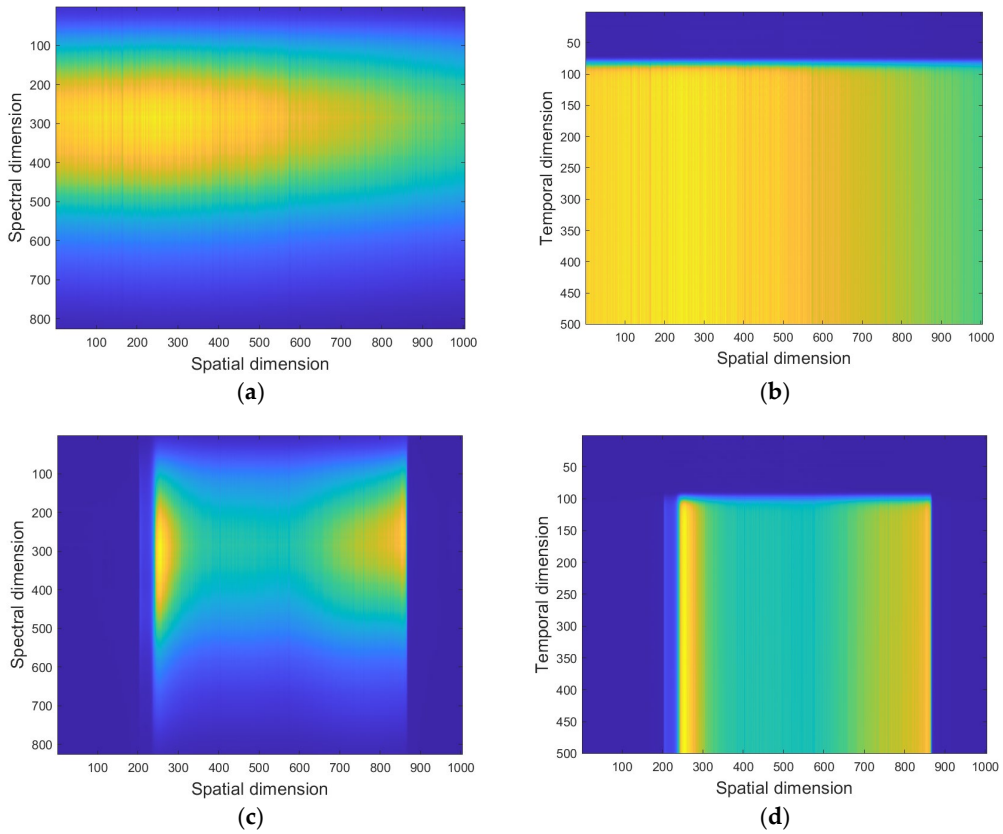

Figure 9. Representation of the HS cube measured for the different illumination conditions reflectance mode and transmittance. (**a**) Pushbroom frame for reflectance illumination. (**b**) Temporal profile for reflectance illumination. (**c**) Pushbroom frame for transmittance illumination. (**d**) Temporal profile for transmittance illumination.

From the two-dimensional profiles shown in Figure 9, it is possible to extract some useful information for representing and measuring some features of the imaging system. We show this information in Figure 10. Firstly, the spectral information, where the light intensity is represented against the different wavelengths, is shown in Figure 10a,d for the reflectance and the transmittance setup, respectively. This information contains both the spectra of the emitting light as well as the spectral response of the instrumentation. Secondly, the mean light intensity for the different spatial pixels is shown. As mentioned before, in the reflectance experiments (Figure 10b), the light is homogeneous within the FOV of the camera. On the contrary, for the transmittance experiments (Figure 10e), the light is only present in the central pixels of the camera FOV (approximately from pixel 250th to pixel 850th). Thirdly, the evolution of the light intensity over time is represented in Figure 10c,f. From these representations, the different stages of our experiments are clearly visualized. In the first seconds of the experiments, the light is turned off (intensity around 0). Then, the light is turned on, and there is a transient period until the light is stabilized. Finally, in the steady period, light intensity is high and constant over time.

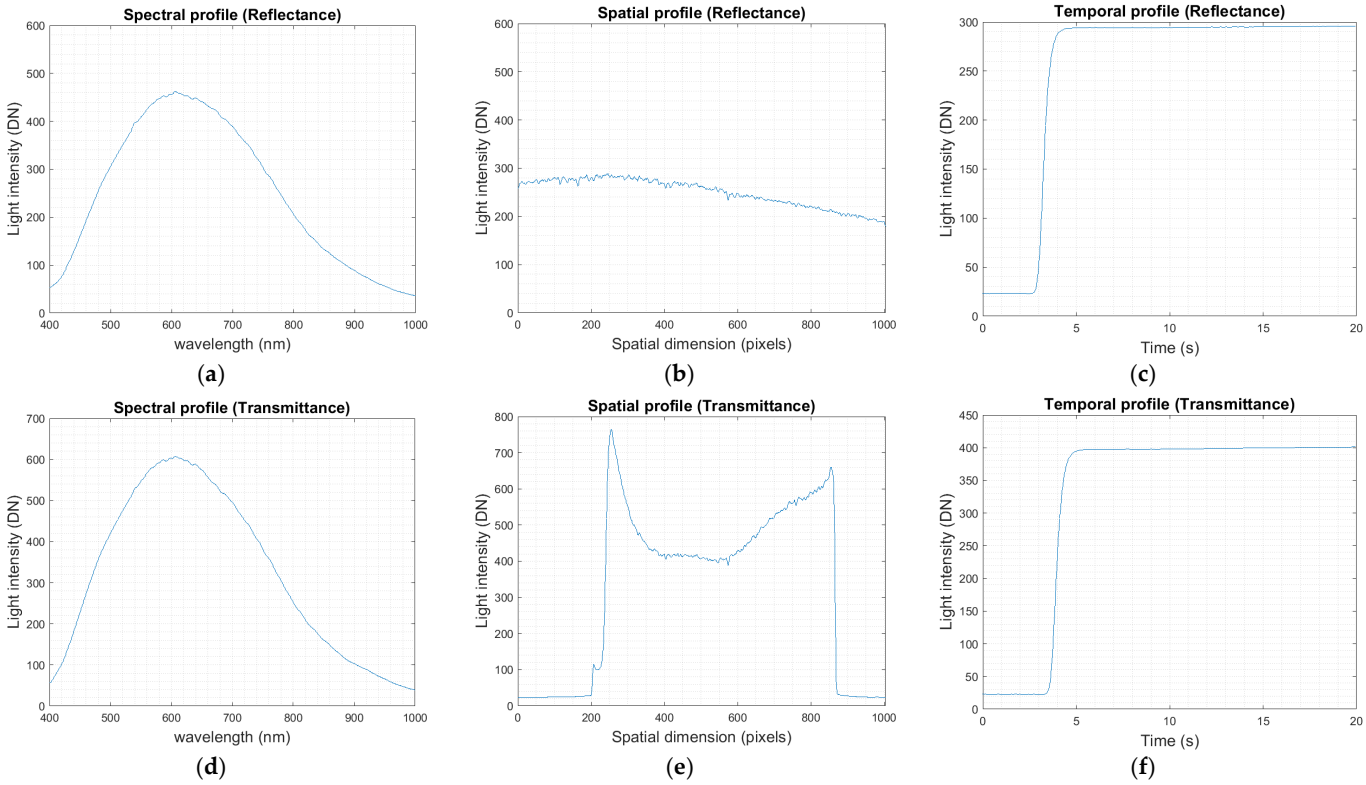

Figure 10. Information extracted from the HS cube for the different illumination modes. (**a**) Reflectance spectral profile. (**b**) Reflectance spatial profile. (**c**) Reflectance temporal profile. (**d**) Transmittance spectral profile. (**e**) Transmittance spatial profile. (**f**) Transmittance temporal profile.

4. Experimental Results

4.1. Performance of the Proposed Power Supply

Using the PSIM 10.0 simulation software (Powersys., Les Jardins de l'Entreprise, BP, France), a schematic of the proposed SMPS with power factor correction was implemented under conditions of maximum power output (300 W). Upon completion of the simulation, the voltage waveform at the input (ideal power grid) and the resulting current waveform were displayed. This visualization also provided additional results, including the PF value and THD. According to the simulations, as shown in Figure 11, the PF is 0.96, and the THD is 2.65%.

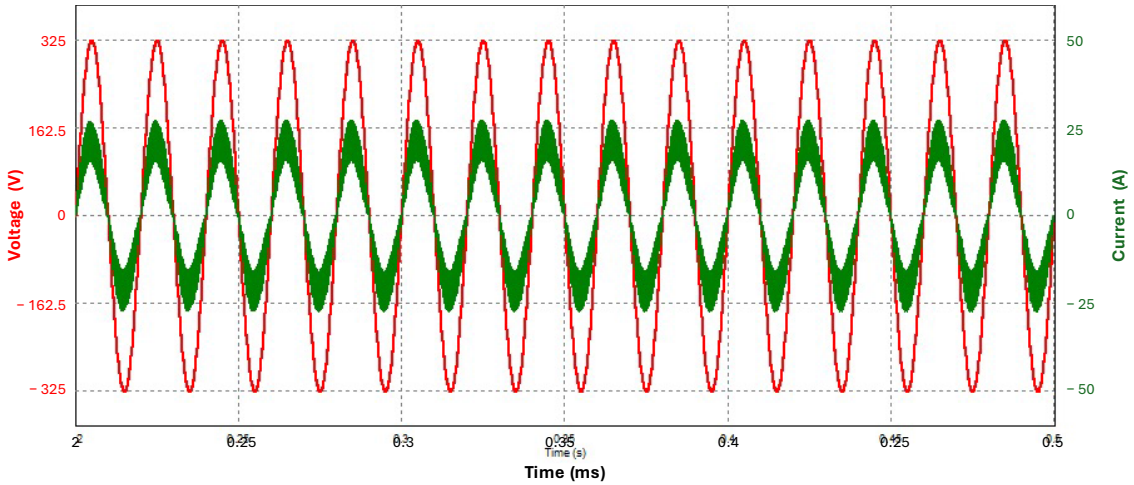

Figure 11. Waveform of the voltage supplied by the grid to the power supply and the resulting current due to the power factor correction. PF = 0.96. THD = 2.65%.

A PF meter (KWS-AC301 Power Meter) was used at the input stage to measure electrical parameters. This meter consisted of a current-sensing toroidal transformer placed around one of the two power supply cables connected to the electrical grid. In parallel, a voltage meter was connected to both power supply cables. A spectrum analyzer (Fluke 1770 Series; Fluke Ibérica, Alcobendas, Madrid, Spain) was employed to assess harmonic distortion and specifically configured to monitor the primary harmonics generated by the system and injected into the electrical grid. This analyzer is capable of calculating the THD and displaying the results on its screen. Finally, for measuring output power, two TRUE RMS digital multimeters (UNI-T UT890C) were used—one to measure the output voltage and the other to measure the output current. The employment of a wattmeter combined with a current shunt would facilitate the acquisition of more precise measurements because it minimizes the introduction of nonlinearities. However, while measurements taken with this type of instrumentation can be influenced by some nonlinearities, they still maintain adequate quality for conducting electrical comparisons between different sources.

The results from these electrical measurements for the three power supplies (the proposed one and two commercial models) are shown in Table 2. Regarding the experimental results, it was observed that the simulation accurately validated the measured values at maximum power. However, at minimum power, there was a noticeable discrepancy between the simulated and actual measured results. This may be due to the simulation model not fully incorporating the complete switching element model. The comparison of the three power supplies leads to the conclusion that the proposed switch-mode power supply with PFC outperforms the commercial models across the entire power range. In fact, it delivers twice the power of either of the commercial units. It was also found that the commercial supplies exhibited higher electrical noise in the lamp, whereas the proposed switch-mode power supply showed significantly improved THD, resulting in a better power factor.

Table 2. Electrical comparative of the different power supplies. PF: power factor, THD: total harmonic distortion; CPS: commercial power supply; PPS: proposed power supply; NA: not applicable.

Output Power	PF			THD		
(W)	CPS1	CPS2	PPS	CPS1	CPS2	PPS
34.6	0.42	0.35	0.69	26.30%	32.00%	3.00%
68.9	0.45	0.51	0.75	24.00%	11.00%	3.00%
150.3	0.52	0.72	**0.82**	21.00%	3.00%	**2.90%**
300	NA	NA	0.96	NA	NA	2.65%

The system's performance can be summarized as follows:

- Output ripple voltage is high but does not affect the illumination efficiency of the lamp because the switching frequency of the output converters is about 3000 times higher than the noise generated by the lamp as it heats up;
- The lamp noise does not increase because the sampling frequency and subsequent corrections are very fast. In contrast, with an LPS, the noise increases because the voltage compensation is relatively slow compared to the noise frequency of the lamp;
- Although the final PF is not constant and fluctuates depending on the power delivered at the output (no commercial power supply is constant, and the PF shown on the datasheet is the best achieved, which coincides with the maximum power at the output), it improves on the PF achievable with passive filters;

- The supplied power was able to reach that value with an efficiency of 93%, but the power consumed from the network was of the order of 1500 VA since the PF was 0.33 due to high harmonic distortion. It was necessary to adopt an automatic control of the PF that substantially improved the PF.

As a result, the following benefits were obtained:

- The input voltage has a low effect on the current loop gain;
- The system is not unstable for duty cycle values lower than 0.5;
- The average value of the current is regulated;
- The system has higher noise immunity because the modulator receives an averaged signal;
- The use of a PF correction integrated circuit (IC) ensures that the network current demand remains sinusoidal. This IC automatically corrects the PF within specified limits by sampling the input voltage (from the power grid) and adjusting the circuit's current to align with the input voltage waveform. It primarily reduces harmonics generated during current rectification by shifting their frequency closer to the IC's switching frequency. The inclusion of this IC (in our case, the UC3854) significantly improves the PF compared to a system without such an IC, which exhibits input currents with substantial harmonic distortion. The PF correction circuit fulfills all the necessary conditions for the SMPS to take advantage of the power provided by the network while minimizing the distortion of the network current.

4.2. Evaluation of Performance for the Hyperspectral Image Application

In this section, we present a comparison of the performance between the different power supplies when used in light sources for hyperspectral imaging. Initially, we implemented data preprocessing techniques designed to extract information from the HS cubes automatically. This automation is crucial for eliminating the need for manual intervention and selective feature extraction. Following the extraction of valuable information from the HS data, we quantified various light parameters for the different power supplies to characterize their performance.

4.2.1. Automatic Extraction of the Spatial Region of Interest for the Transmittance Mode

As mentioned in the previous section, the light is limited to a finite region within the camera FOV for the transmittance illumination mode. For that reason, it is necessary to perform a selection of that region of interest (ROI) within the spatial dimension for the subsequent analysis. To perform this automatically, we made use of image processing techniques. In this case, in order to automatically locate the light in the ROI, we calculated the derivative of the spatial profile of the light intensity (Figure 10e). The derivative is shown in Figure 12a. The maximum and minimum values of such derivative indicate the maximum positive and negative slopes of the spatial profile, and hence, such information can be used to identify the spatial location of the backlight illuminator (Figure 12b). Finally, this information was used to extract the pixels where there is light intensity (Figure 12c). After applying this method, we were able to accurately identify the position of the light within the camera's field of view and focus the analysis on that particular area.

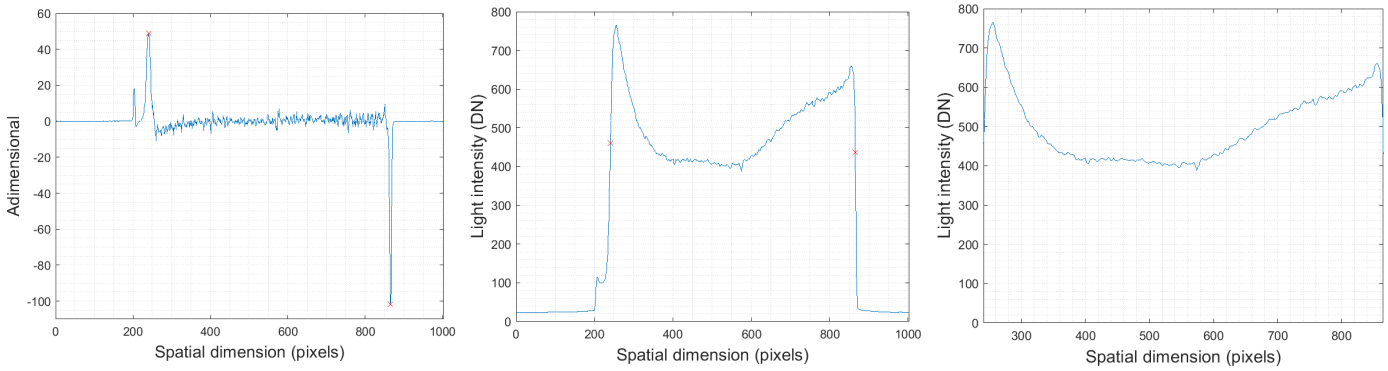

(**a**) (**b**) (**c**)

Figure 12. Automatic identification of the spatial location of the light source in transmittance mode. (**a**) Derivative extracted from the spatial profile. (**b**) Selection of the region of interest (red crosses) within the spatial profile using the information from the derivative. (**c**) Spatial profile from the region of interest.

4.2.2. Automatic Extraction of the Light-Intensity Values Within the Steady Period

In order to facilitate the analysis of the data for the quantification of different parameters of the light sources, it would be beneficial to have an automatic extraction of the different time stages of the light intensity. It is interesting to automatically locate the transient and steady periods within the light-intensity profile (Figure 13a). Taking advantage of the different light intensities for the different stages of the proposed experiments, we made use of a histogram in order to automatically identify such areas. In the histogram shown in Figure 13b, it can be observed that there are two regions with a high presence of pixel counts. The low intensity values of such histogram represent the period when the light is turned off, while the high light-intensity values correspond to the period during which the light is on (steady period). The intermediate light-intensity values correspond to the transient period. Using this information and a thresholding method, it was possible to automatically identify the different temporal stages of the experiment, as shown in Figure 13c.

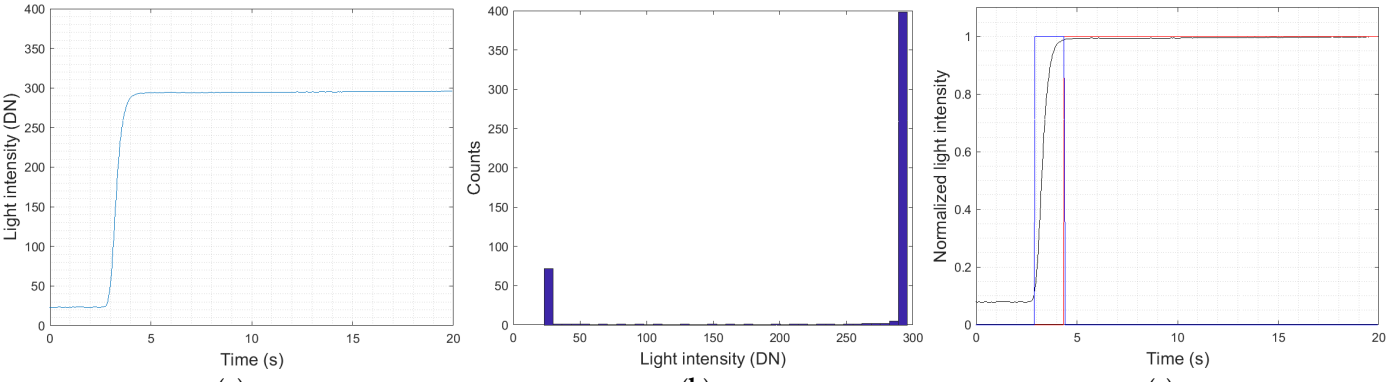

(**a**) (**b**) (**c**)

Figure 13. Automatic identification of the transient region for the experiments. (**a**) Light profile. (**b**) Histogram from the light profile. (**c**) Identification of the steady period (blue) and the transient period (red) from the light profile (black).

Once this process was applied to every image in the dataset, there were different light-intensity profiles for each power supply model (PPS, CPS1, and CPS2) and for each illumination mode (reflectance and transmittance), as shown in the examples of Figure 14. The specific details concerning the features of the different power supplies based on their light-intensity profiles are discussed later in the manuscript. However, some differences

can be directly observed from Figure 14. The transient period is shorter for CLS-1 compared to PLS and CLS-2. Meanwhile, although the light intensity seems to remain constant during the steady period for PLS and CLS-2, the light profile of CLS-1 shows a slight decrease over time.

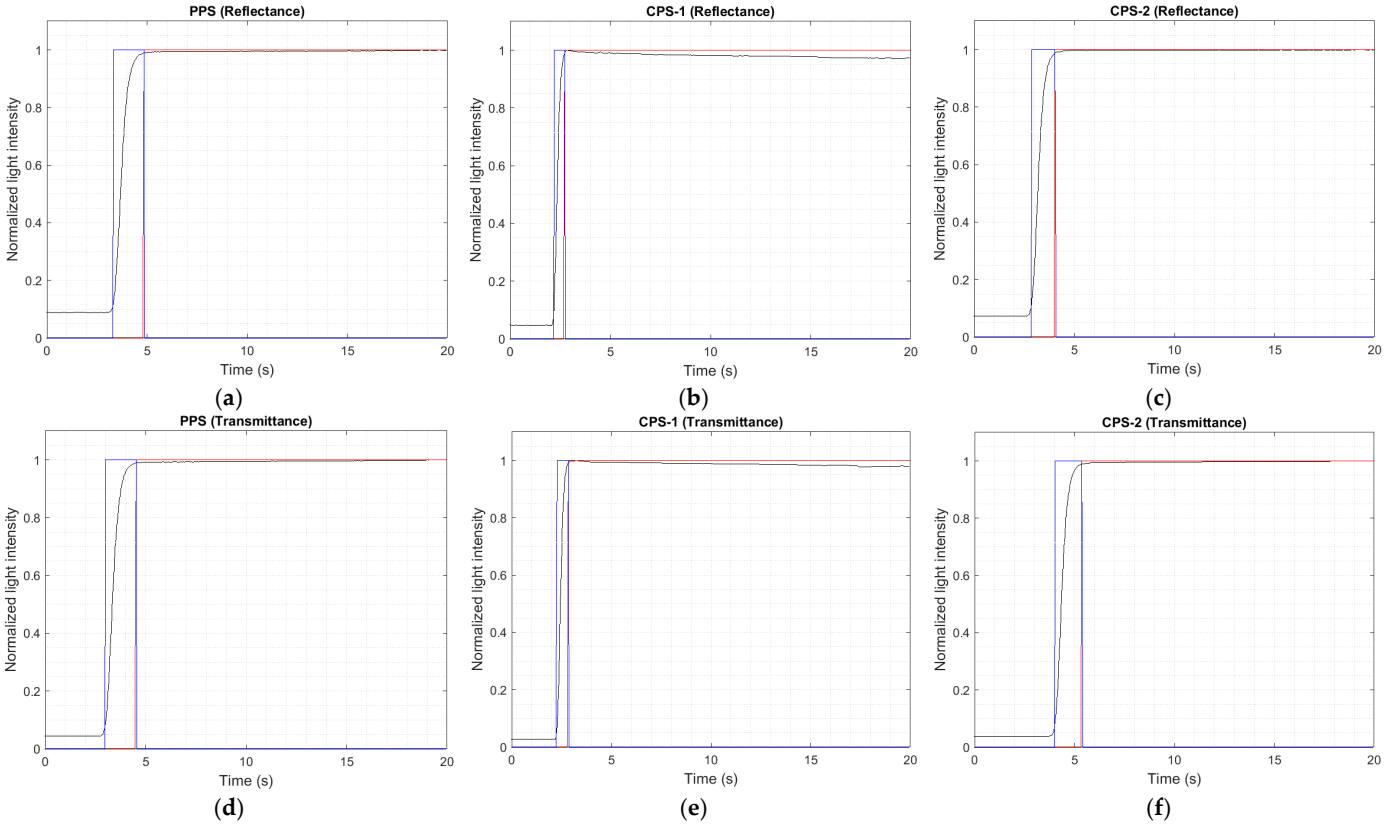

Figure 14. Examples of the light profiles provided for the different light sources and illumination modes. (**a**) PLS reflectance. (**b**) CLS1 reflectance. (**c**) CLS2 reflectance. (**d**) PLS transmittance. (**e**) CLS1 transmittance. (**f**) CLS2 transmittance.

4.2.3. Steady Period Evaluation

In order to perform a comparison between the different steady periods for the different light sources and illumination modes, a boxplot is presented in Figure 15 (data available in Supplementary Materials, Table S1). The boxplot is generated using the ten repeated measurements made for every power supply in each illumination mode. In this boxplot, it can be observed that the shortest steady period is provided by CLS-1, and the longest steady period is provided by PLS. Additionally, it can be observed that the mean steady period trend is similar for the different illumination modes (reflectance and transmittance). However, the standard deviation of the steady period seems to be higher in the transmittance illumination mode. The measurement of the steady period supposes a useful tool for the comparison of the electrical performance of the different light sources. However, in the application of this light source for many HSI applications, the steady period is not relevant since the operator will wait a few minutes before the image acquisition, and the worst steady time for these lamps is lower than 2 s. In any case, for situations that require a fast light response, it is important to know the steady times of the different lamps.

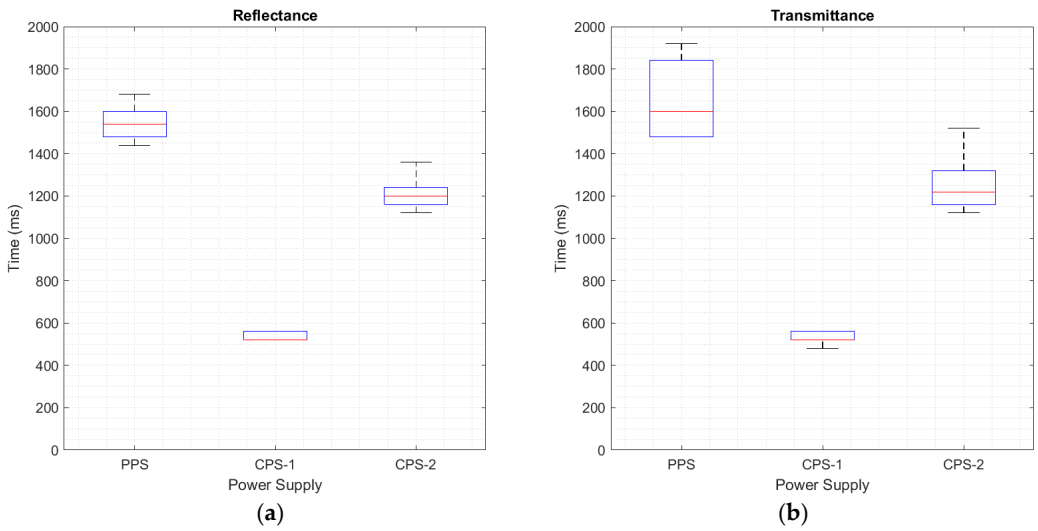

Figure 15. Steady time for the different types of power supplies (PPS, CPS-1, and CPS-2). (**a**) Reflectance mode. (**b**) Transmittance mode.

4.2.4. Light Stability Evaluation

After analyzing the transient behavior of various power supplies by measuring their steady time, the next step was to evaluate their performance during the steady state. Our focus was on assessing the stability of the light signal, which involves measuring the variation in light intensity over time. To accurately quantify this stability, we examined the spread of light-intensity values over time, typically using the standard deviation. However, the standard deviation is affected by the mean light-intensity value, and our experimental setup did not allow for uniform electrical power output for each light source under evaluation. Therefore, we employed the coefficient of variation, which is the ratio of the standard deviation to the mean, as a more effective metric for comparing variables sources with varying mean intensities. For this purpose, we used the inverse of the coefficient of variation as our stability metric, providing a measure of light stability with high values when there are smaller variations in light intensity over time.

In signal processing and image processing, the ratio between the mean and the standard deviation is known as the signal-to-noise ratio (SNR), and we used this metric for quantifying light stability. The SNR was calculated according to Equation (10), where μ and σ refer to the mean and the standard deviation of the light intensity over time ($light$). In this case, the mean light intensity across the different wavelength was used. To ensure a reliable quantification of light stability, the SNR was determined using the data from the final 10 s of each measurement, providing a safety margin beyond the point at which steady state was achieved.

$$SNR\ (dB) = 20log_{10}\left(\frac{\mu(light)}{\sigma(light)}\right) \quad (10)$$

The light stability in terms of the SNR for the different power supplies and illumination modes is presented in Figure 16 (data available in Supplementary Materials, Table S1). The boxplot reveals that all tested power supplies maintained a high SNR exceeding 45 dB, indicating robust light stability independently of the power supply. However, there are differences in SNR between the different power supplies. When comparing the performance of the different power supplies, CPS-2 exhibited the superior SNR, while CPS-1 showed the inferior SNR. The performance of the power supply developed in this study (PPS) falls between those of two commercial power supplies. To quantify the differences in SNR presented in Figure 16 for the different power supplies, we performed a statistical analysis on the data. Initially, we assessed the normality of the data using the Shapiro–

Wilk Test, which indicated that the data did not follow a normal distribution. Consequently, we conducted a Kruskal–Wallis test, a non-parametric alternative to ANOVA, appropriate for cases where the normality assumption is not satisfied. This test was used to evaluate whether there were significant differences in SNR across the different power supplies. The results of the Kruskal–Wallis test revealed significant effects for reflectance measurements (H-statistic = 24.58, p-value = 4.60×10^{-6}) and for transmittance measurements (H-statistic = 23.69, p-value = 7.16×10^{-6}). These findings suggest that at least one power supply exhibited a significantly different SNR compared to the others. To identify which specific power supplies showed significant differences, we applied Dunn's post hoc test. For reflectance measurements, Dunn's test indicated significant differences between CPS-1 and CPS-2 ($p < 0.0001$) as well as between PPS and CPS-1 ($p = 0.02296$), while no significant difference was observed between PPS and CPS-2 ($p = 0.06676$). In terms of transmittance measurements, Dunn's test showed significant differences between CPS-1 and CPS-2 ($p < 0.0001$) and between PPS and CPS-2 ($p = 0.0169$) but found no significant difference between PPS and CPS-1 ($p = 0.1118$). In summary, our results indicate a mix of significant and non-significant differences depending on both the power supply and the mode of illumination. This suggests that both the illumination system and the power supply play a crucial role in the performance of hyperspectral imaging systems.

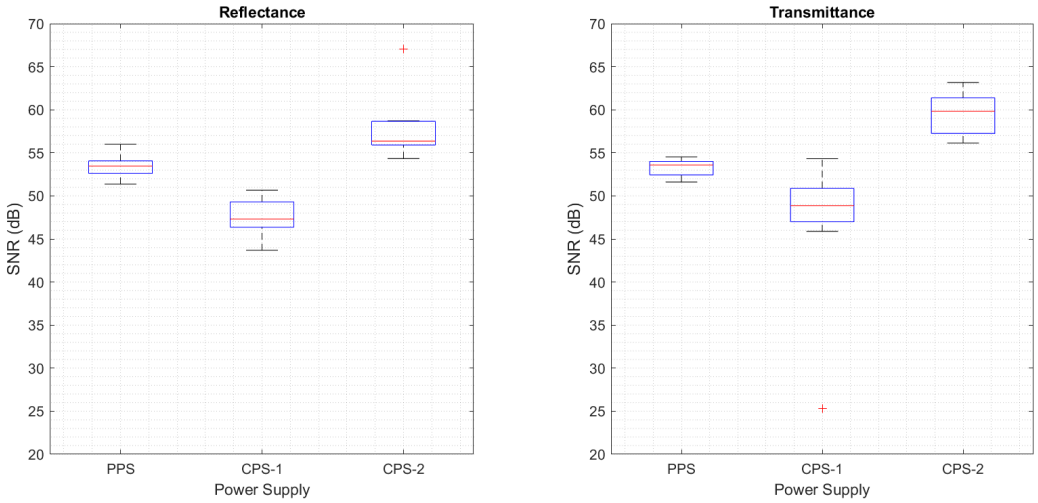

Figure 16. Light stability (SNR) for the different types of power supplies (PPS, CPS-1, and CPS-2). (**a**) Reflectance mode. (**b**) Transmittance mode.

The light stability shown in Figure 16 represents the average light intensity across the entire spectral range captured by the HS camera. To study how light stability varies across different wavelengths, we computed the light stability for each spectral band of the instrument (Figure 17). This approach allows for a comprehensive understanding of the light stability performance across the spectrum, highlighting the wavelength-specific variations in light-intensity stability. The observed pattern in the SNR for the average light intensity remained consistent across different power supplies. However, there was a noticeable dependency of light stability on the wavelength for the power supplies light sources under evaluation as well as variations depending on the illumination modes.

In reflectance measurements (Figure 17a), PPS displayed a SNR over 50 dB from roughly 450 to 800 nm, peaking at 600 nm (55.5 dB). CPS-2 outperformed with a SNR above 50 dB spanning from 450 to 850 nm and its highest SNR at 600 nm (60 dB). CPS-1 exhibited a unique performance, maintaining an SNR above 50 dB from 620 to 850 nm, with its peak at 780 nm (54 dB). CPS-1 achieved the optimal SNR between 800 and 880 nm. Across all power supplies, the SNR was comparable from 900 to 1000 nm.

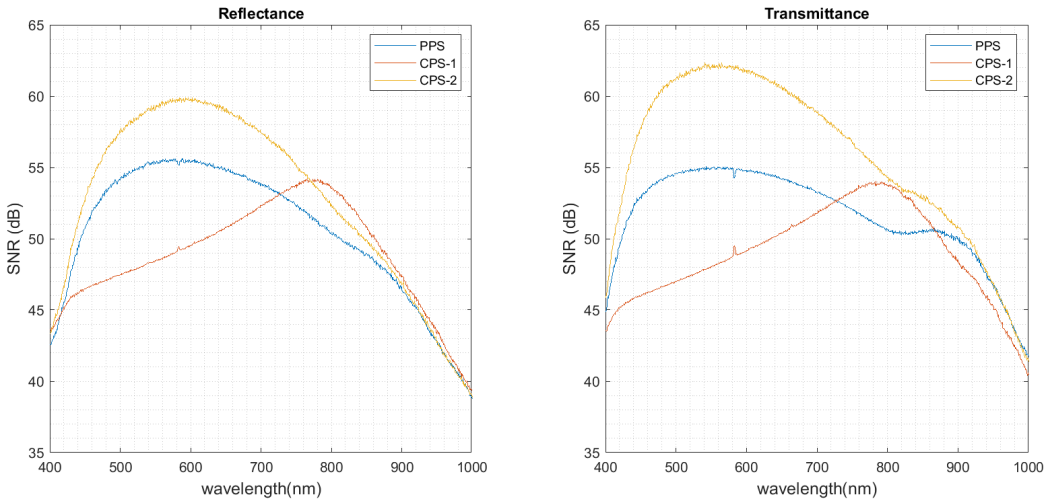

Figure 17. Light stability (SNR) across spectral bands for the different type of power supplies (PPS, CPS-1, and CPS-2). (**a**) Reflectance mode. (**b**) Transmittance mode.

In the transmittance measurements in Figure 17b, PPS shows a SNR of 50 dB across the 440 to 900 nm wavelength range, peaking at 560 nm (55 dB). CPS-2 surpasses the others by maintaining an SNR above 50 dB from 420 to 920 nm, reaching its highest at 560 nm (62 dB). CPS-1, on the other hand, achieves an SNR greater than 50 dB between 640 and 860 nm, with its peak at 790 nm (54 dB). In this case, CPS-2 offers the best SNR across the entire spectrum, while CPS-1 outperforms PPS in the 730 to 860 nm range. From 920 to 1000 nm, PPS and CPS-2 demonstrate comparable SNR levels, while CPS-1 falls behind.

According to our observations, the SNR measurements tend to be higher across the spectral range for transmittance illumination compared to reflectance, indicating that the type of illumination head has an impact on the overall light stability. However, the primary factor influencing light stability within the studied spectral range is attributed to the power supply used. Both the PPS and CPS-2 power supplies exhibit consistently high SNR across the entire spectral range. In contrast, the CPS-1 power supply demonstrates superior performance in the infrared spectral range (from 700 nm) but shows decreased performance in the visible spectral range (from 400 to 700 nm). Since the only differences in the different measurements is the power supply, these findings emphasize the critical importance of selecting an appropriate power supply for HSI systems, as the type of power supply can lead to notable differences in lighting performance.

5. Conclusions

This paper shows the performance of a custom regulated power supply integrated into an HS acquisition system considering different light-intensity profiles for three types of lamps and two illumination modes. Detailed results are provided for steady period and light stability, showing better performance of the 150 W custom power supply (PPS) and TechniQuip's commercial power supply (CPS-2) with respect to the MI-150 fiber optic illuminator (CPS-1) in terms of light stability; however, steady period is minimized considering the fiber optic illuminator. Moreover, the automatic extraction of the spatial ROI for the transmittance mode together with the automatic extraction of the light-intensity values within the steady period are also presented.

This work analyzes the effects of different power supplies when applied to hyperspectral illumination. It has been shown that the quality of the power supply affects the quality of the resulting light at different wavelengths, but little research has been performed on the effect of the design of the power supply on the resulting illumination. The

results of our experiments indicate a significant influence of the power supply on the stability of light as measured by the SNR. This effect becomes particularly pronounced when analyzing the SNR across different spectral bands. Power sources with the highest PF and THD, specifically CPS-2 and PPS (as shown in Table 2), also exhibited the best light stability across the spectral range of the camera (Figure 17). However, other factors may also affect SNR, highlighting the need for further research to clarify the extent to which PF and THD affect light stability across various wavelengths. Considering these findings, future research should aim to identify which components of the power supply contribute to either positive or negative impacts on the SNR at various wavelengths. Specifically, it should focus on AC/DC converters used in lamp power supplies, which are known for exhibiting significant non-linearity. Additionally, future research should benchmark the performance of different real-world power supplies against an ideal power supply, i.e., one that provides a pure sine wave with minimal series impedance. This comparison would offer a more reliable reference for future studies in this area.

Furthermore, it is necessary to understand the importance of SNR in specific HSI applications, identifying scenarios where high SNR is required and selecting an appropriate power supply accordingly. To effectively address specific challenges in HSI, such as classification or segmentation, additional experiments are necessary. This can be achieved by creating datasets consisting of the same objects illuminated using different power supply configurations. Then, the impact of different illumination conditions on the specific problems being studied could be evaluated. The effects of different lighting conditions will be considered for future research. Finally, while this study was concentrated on evaluating light stability in the VNIR spectral range, future research should expand to include higher spectral regions (beyond 1000 nm), which are crucial for a wide range of HSI applications.

Supplementary Materials: The following supporting information can be downloaded at www.mdpi.com/article/10.3390/app15031093/s1. Figure S1: Schematic of the step-down converter with output voltage sampling and input current sampling compensation. Table S1: Results for the steady time and SNR for the different types of power supplies (PPS, CPS-1, and CPS-2), in reflectance and transmittance mode.

Author Contributions: Conceptualization, J.M.C.-P., S.O., H.F. and G.M.C.; methodology, J.M.C.-P., R.L., S.O. and H.F.; validation, R.L. and S.O.; formal analysis, R.L., E.Q. and S.O.; investigation, J.M.C.-P., R.L. and S.O.; resources, J.M.C.-P. and G.M.C.; writing—original draft preparation, J.M.C.-P., R.L., S.O. and H.F.; writing—review and editing, E.Q. and G.M.C.; visualization, H.F.; supervision, G.M.C.; project administration, G.M.C.; funding acquisition, J.M.C.-P. and G.M.C. All authors have read and agreed to the published version of the manuscript.

Funding: This work has been supported by Spanish Government and European Union (FEDER funds) as part of (i) TALENT-HExPERIA (HypErsPEctRal Imaging for Artificial intelligence applications) project with ref. PID2020-116417 RB-C42 and (ii) OASIS (Open AI-Driven stack para plataformas HPEC mejoradas en sistemas integrados) project with ref. PID2023-148285OB-C43. Additionally, this work was completed while Raquel Leon was beneficiary of a pre-doctoral grant given by the "Agencia Canaria de Investigacion, Innovacion y Sociedad de la Información (ACIISI)" of the "Consejería de Economía, Conocimiento y Empleo" of the "Gobierno de Canarias", which is part-financed by the European Social Fund (FSE) (POC 2014-2020, Eje 3 Tema Prioritario 74 (85%)).

Data Availability Statement: Not applicable.

Conflicts of Interest: The authors declare no conflicts of interest.

References

1. Qian, S.-E. Hyperspectral Satellites, Evolution, and Development History. *IEEE J. Sel. Top. Appl. Earth Obs. Remote Sens.* **2021**, *14*, 7032–7056. https://doi.org/10.1109/JSTARS.2021.3090256.
2. Goetz, A.F.H. Three Decades of Hyperspectral Remote Sensing of the Earth: A Personal View. *Remote Sens. Environ.* **2009**, *113*, S5–S16. https://doi.org/10.1016/j.rse.2007.12.014.
3. Jia, W.; van Ruth, S.; Scollan, N.; Koidis, A. Hyperspectral Imaging (HSI) for Meat Quality Evaluation across the Supply Chain: Current and Future Trends. *Curr. Res. Food Sci.* **2022**, *5*, 1017–1027. https://doi.org/10.1016/j.crfs.2022.05.016.
4. Ortega, S.; Lindberg, S.-K.; Anderssen, K.E.; Heia, K. Perspective Chapter: Hyperspectral Imaging for the Analysis of Seafood. In *Hyperspectral Imaging—A Perspective on Recent Advances and Applications*; Huang, J.Y., Ed.; IntechOpen: Rijeka, Croatia, 2022.
5. Cucci, C.; Casini, A. Hyperspectral Imaging for Artworks Investigation. In *Hyperspectral Imaging*; Elsevier: Amsterdam, The Netherlands, 2019; pp. 583–604.
6. Grabowski, B.; Masarczyk, W.; Głomb, P.; Mendys, A. Automatic Pigment Identification from Hyperspectral Data. *J. Cult. Herit.* **2018**, *31*, 1–12. https://doi.org/10.1016/j.culher.2018.01.003.
7. Zheng, Y.; Bai, J.; Xu, J.; Li, X.; Zhang, Y. A Discrimination Model in Waste Plastics Sorting Using NIR Hyperspectral Imaging System. *Waste Manag.* **2018**, *72*, 87–98. https://doi.org/10.1016/j.wasman.2017.10.015.
8. de Cássia Mariotti, K.; Ortiz, R.S.; Ferrão, M.F. Hyperspectral Imaging in Forensic Science: An Overview of Major Application Areas. *Sci. Justice* **2023**, *63*, 387–395. https://doi.org/10.1016/j.scijus.2023.04.003.
9. Fei, B. Hyperspectral Imaging in Medical Applications. In *Hyperspectral Imaging*; Elsevier: Amsterdam, The Netherlands, 2020; pp. 523–565.
10. Khan, U.; Paheding, S.; Elkin, C.P.; Devabhaktuni, V.K. Trends in Deep Learning for Medical Hyperspectral Image Analysis. *IEEE Access* **2021**, *9*, 79534–79548. https://doi.org/10.1109/ACCESS.2021.3068392.
11. Ortega, S.; Guerra, R.; Diaz, M.; Fabelo, H.; Lopez, S.; Callico, G.M.; Sarmiento, R. Hyperspectral Push-Broom Microscope Development and Characterization. *IEEE Access* **2019**, *7*, 122473–122491. https://doi.org/10.1109/ACCESS.2019.2937729.
12. Echávarri-Dublhán, J.; Alonso-Santamaría, M.; Luri-Esplandiú, P.; Sháiz-Abajo, M.-J. Comparison of Different Illumination Systems for Moisture Prediction in Cereal Bars Using Hyperspectral Imaging Technology. *J. Spectr. Imaging Volume 11*, a10 **2022**. https://doi.org/10.1255/jsi.2022.a10.
13. Sawyer, T.W.; Luthman, A.S.; Bohndiek, S.E. Evaluation of Illumination System Uniformity for Wide-Field Biomedical Hyperspectral Imaging. *J. Opt.* **2017**, *19*, 045301. https://doi.org/10.1088/2040-8986/aa6176.
14. Katrašnik, J.; Pernuš, F.; Likar, B. A Method for Characterizing Illumination Systems for Hyperspectral Imaging. *Opt. Express* **2013**, *21*, 4841. https://doi.org/10.1364/OE.21.004841.
15. Manea, D.; Calin, M.A. Hyperspectral Imaging in Different Light Conditions. *Imaging Sci. J.* **2015**, *63*, 214–219. https://doi.org/10.1179/1743131X15Y.0000000001.
16. Zahavi, A.; Palshin, A.; Liyanage, D.C.; Tamre, M. Influence of Illumination Sources on Hyperspectral Imaging. In Proceedings of the 2019 20th International Conference on Research and Education in Mechatronics (REM), Wels, Austria, 23–24 May 2019; IEEE: Piscataway, NJ, USA, 2019; pp. 1–5.
17. Geladi, P.; Burger, J.; Lestander, T. Hyperspectral Imaging: Calibration Problems and Solutions. *Chemom. Intell. Lab. Syst.* **2004**, *72*, 209–217. https://doi.org/10.1016/j.chemolab.2004.01.023.
18. *IEEE Std 519-2022 (Revision of IEEE Std 519-2014)*; IEEE Standard for Harmonic Control in Electric Power Systems. IEEE: Piscataway, NJ, USA, 2022; pp. 1–31. https://doi.org/10.1109/IEEESTD.2022.9848440.
19. Ben-Yaakov, S.; Peretz, M.M.; Hesterman, B. A SPICE Compatible Behavioral Electrical Model of a Heated Tungsten Filament. In Proceedings of the Twentieth Annual IEEE Applied Power Electronics Conference and Exposition, Austin, TX, USA, 6–10 March 2005; IEEE: Piscataway, NJ, USA, 2005; Volume 2, pp. 1079–1084.
20. UNE-EN IEC 61000-3-2:2019. (2019). Electromagnetic compatibility (EMC)—Limits for harmonic current emissions (equipment input current ≤ 16 A per phase). International Electrotechnical Commission. https://www.iec.ch
21. Duncombe, J.U. Infrared Navigation—Part I: An Assessment of Feasibility. *IEEE Trans. Electron Devices* **1959**, *11*, 34–39.